Probing particle size dependency of frequency mixing magnetic detection with dynamic relaxation simulation

Ulrich M. Engelmann[1*], Ali Mohammad Pourshahidi[2,3], Ahmed Shalaby[1] and Hans-Joachim Krause[3,4*]

[1] Medical Engineering and Applied Mathematics, FH Aachen University of Applied Sciences, 52428 Jülich, Germany
[2] Faculty of Mathematics, Computer Science and Natural Sciences, RWTH Aachen University, 52062 Aachen, Germany
[3] Institute of Biological Information Processing , Bioelectronics (IBI-3), Forschungszentrum Jülich, 52428 Jülich, Germany
[4] Institute of Nano- and Biotechnologies (INB), FH Aachen University of Applied Sciences, 52428 Jülich, Germany

[*]Correspondance: engelmann@fh-aachen.de (UME) | h.-j.krause@fz-juelich.de (HJK)

Keywords:
Biosensing, frequency mixing magnetic detection, magnetic nanoparticles, magnetic relaxation magnetic simulation, non-linear Néel-Brown relaxation dynamics, size dependency

Abstract
Biomedical applications of magnetic nanoparticles (MNP) fundamentally rely on the particles' magnetic relaxation as a response to an alternating magnetic field. The magnetic relaxation complexly depends on the interplay of MNP magnetic and physical properties with the applied field parameters. It is commonly accepted that particle core size is a major contributor to signal generation in all the above applications, however, most MNP samples comprise broad distribution spanning 10 nm and more. Therefore, precise knowledge of the exact contribution of individual core sizes to signal generation is desired for optimal MNP design generally for each application. Specifically, we present a magnetic relaxation simulation-driven analysis of experimental frequency mixing magnetic detection (FMMD) for biosensing to quantify the contributions of individual core size fractions towards signal generation. Applying our method to two different experimental MNP systems, we found the most dominant contributions from approx. 20 nm sized particles in the two independent MNP systems. Additional comparison between freely suspended and immobilized MNP also reveals insight in the MNP microstructure, allowing to use FMMD for MNP characterization, as well as to further fine-tune its applicability in biosensing.

1 Introduction

Magnetic Nanoparticles (MNP) are being widely researched for frequency-dependent biomedical applications [1–3] in diagnostics such as magnetic resonance imaging (MRI) and magnetic particle imaging (MPI) as well as in therapy [4,5] using magnetic fluid hyperthermia (MFH). As of recent, the combination of both diagnostic MPI and therapeutic MFH applicability was researched [6] and early feasibility has been successfully demonstrated [7,8]. Beyond these promising research examples noted above, MNP are also showing high potential as biomarkers for biomolecules in immunoassays. Here, established techniques such as AC-susceptibility [9] and relaxometry [10], are being increasingly complemented by the emerging frequency mixing magnetic detection (FMMD) technique [11]. FMMD achieves high detection sensitivity by using dual frequency excitation of the MNP employing a high-frequency/low-amplitude excitation field superimposed on a low-frequency/high-amplitude driving field [12]. FMMD has been successfully demonstrated to reliably detect analytes such as viruses [13], antibiotics [14] and bacterial toxins [15].

The majority of the applications noted above rely heavily on the relaxation of the MNP within the applied excitation frequencies, which is particle core size dependent [16,17]. Theoretical and experimental research on the core size dependency of MPI [18–20] and MFH [21–24] has been extensive. However, there is no such research for FMMD as of now. Furthermore, there is an ongoing discussion which particle properties are best suited for any specific application [1,4,25]. The main reason for this ambiguity lies in the multidimensional effects that the core size has on the desired effect in the specific application, either directly (e.g. on magnetic relaxation, iron content per particle and magnetization) and/or indirectly (e.g. on magnetic anisotropy constant, local iron concentration and hydrodynamic size). As tailor-made MNP are limited and costly [16], state-of-the-art magnetic relaxation dynamics simulations are commonly being used to predetermine optimal MNP properties for MPI and MFH application [20,24,26]. However, despite existing counter-examples [27–29], simulations are often presented stand-alone, missing direct validation against experimental results and thus their predictive power is questionable and/or limited for applications, as discussed most recently for e.g. MFH [30].

In the present study, we demonstrate how state-of-the-art magnetic relaxation dynamics simulations can be adapted and implemented to quantify the size-dependent contributions to the overall signal generation of an experimental FMMD measurement. The method is robust, as it is readily applicable to two different types of MNP (Perimag and Nanomag-D), and is able to provide further insight into the MNP properties at microscale. Furthermore, the results serve as a major validation step towards using the presented simulations as a stand-alone methodology to predict optimal MNP properties for advanced FMMD-based biosensing in the future.

2 Simulation

2.1 Physical description of non-linear Néel-Brown magnetic relaxation dynamics

We model the MNP relaxation dynamics under non-equilibrium conditions using combined Néel-Brown relaxation dynamics, as described in detail previously [20,24]. The magnetic moment of a single MNP, $\boldsymbol{m}_p$, evolves with Néel relaxation under an applied AMF, $\boldsymbol{H}$ (cf. eq. 4), according to the Landau-Lifshitz-Gilbert equation (LLG) [31]:

$$\frac{d\boldsymbol{m}_p}{dt} = \frac{\mu_0 \gamma}{1+\alpha^2} \cdot \left(\boldsymbol{H}_{\text{eff}} \times \boldsymbol{m}_p + \alpha \boldsymbol{m}_p \times \left(\boldsymbol{H}_{\text{eff}} \times \boldsymbol{m}_p \right) \right) \qquad (1)$$

with the permeability of free space, μ_0, the electron gyromagnetic ratio, γ, the damping parameter, α, and the effective field $\boldsymbol{H}_{\text{eff}}$**.** The easy axis of the MNP, $\boldsymbol{n}$, evolves via Brownian rotation and is described by a generalized torque, $\boldsymbol{\Theta}$ [32]:

$$\frac{d\boldsymbol{n}}{dt} = \frac{\boldsymbol{\Theta}}{6\eta V_H} \times \boldsymbol{n} \qquad (2)$$

with the carrier matrix viscosity, η, and the MNP hydrodynamic volume, $V_h = \pi/6 \cdot d_h^3$, in which d_h is the hydrodynamic particle diameter. The Néel relaxation and Brownian rotation are combined in the internal particle energy:

$$U = -\mu_0 \cdot m_p(\boldsymbol{m}_p \cdot \boldsymbol{H}) - K \cdot V_c(\boldsymbol{m}_p \cdot \boldsymbol{n})^2 + \varepsilon_{IA} \qquad (3)$$

where $m_p = |\mathbf{m}_\mathrm{p}| = V_c \cdot M_S$ is the magnitude of the MNP magnetic moment, and $V_c = \pi/6 \cdot d_c^3$ is the MNP core volume. The first term summarizes the Zeeman energy including the applied field $\boldsymbol{H}$. The second term describes the magnetic anisotropy energy via the effective anisotropy constant, K, assuming uniaxial anisotropy and spherically shaped particles. The third term incorporates the magnetic dipole-dipole interaction among MNP. However, in our case, particle-particle interaction is negligible, as the thermal energy E_{therm} dominates magnetic interaction energy, E_{IA}, by two orders of magnitude in our MNP samples (i.e. $E_{IA} \ll E_{\text{therm}}$) for a number of particles $c < 10^{15}\,\frac{1}{\text{ml}}$. For the given particles with $c \sim 10^{13}\,\frac{1}{\text{ml}}$ (s. Table 1), we neglect particle-particle interactions further on. Please refer to our previous work for a detailed estimation of the effect of magnetic dipole-dipole interaction energy that corroborates our assumption [4,33]. Further details on the full numerical description and implementation of our simulation method are described in our previous works [4,24,25,33].

2.2 Simulation implementation

Relaxation dynamics simulations used 1,000 particles simultaneously, with the magnetization vector and easy axes of each MNP initialized in randomized directions and then thermalized for 1/5 of the total number of time steps, N, before the magnetic field was applied. We used $N = 850{,}000$ and averaged the resulting magnetization over 5 independent simulation runs to achieve a suitable compromise between accuracy and acceptable computation time. The time step sizes then translate to less than 1 ns. Simulations were performed on a cluster computer consisting of 2x Intel Xeon 8168 CPUs with 2.7/3.7 GHz and 24 cores each and 768 GB total RAM at 2666 MHz.

3 Material and methods

3.1 Frequency Mixing Magnetic Detection (FMMD) Setup

The custom-built FMMD setup for simultaneous sample excitation and signal detection comprises two excitation coils and differentially wound pick-up coils for directly recording the digital frequency demodulations for each measurement. The experimental details can be found in our previous works [12,34,35]. The magnetic excitation field is described mathematically as

$$H(t) = H_0 + H_1 \sin(2\pi f_1 t) + H_2 \sin(2\pi f_2 t) \qquad (4)$$

with the experimental parameters chosen as $H_0 = (0, \ldots, 24)$ mT/μ_0 for the static offset field (1 mT/μ_0 step size), $f_1 = 136$ Hz and $H_1 = 14.55$ mT/μ_0 for the low-frequency excitation field and $f_2 = 40\,545$ Hz and $H_2 = 1.25$ mT/μ_0 for the high-frequency excitation field.

Both real and imaginary part of the first four nonlinear magnetic moment demodulations ($f_1 + n \cdot f_2$ with $n = 1,2,3,4$) are recorded. Before each measurement, a reference measurement with no sample installed is performed and used for background subtraction with phase correction of frequency-dependent phase shifts in post-processing of data. Please note that resistive heating inside the coil increased the temperature T in the measurement head from ambient conditions to approximately 310 K, which is also considered in simulations (s. Table 2).

3.2 Sample preparation

Two types of commercially available MNP were used: nanomag-D-SPIO and perimag (both available from Micromod Partikeltechnologie GmbH, Rostock, Germany; product codes 79-19-102 and 102-00-132, respectively). They were characterized according to the manufacturer's data sheet with the following parameters (Table 1).

Table 1. Properties of the MNP stock solutions used for experimental studies.

Particle Type	Hydrodynamic size d_H [nm]	Poly-dispersity index (PDI)	Particle concentration [mg/mL]	Particles per mL	Coating
Perimag	130	< 0.25	25	$1.6 \cdot 10^{13}$	Dextran
Nanomag-D-spio	100	< 0.25	5	$4.3 \cdot 10^{13}$	Dextran

Of each type of MNP, a liquid sample of particles freely dispersed in water suspension, and a sample with particles immobilized on filters were prepared for FMMD measurement as follows: 20 µL of MNP stock solution was diluted in 280 µL of Milli-Q water. Half of the suspension was set aside as the liquid sample. The other half was dried on 5x5 polyethylene filters (Senova Immunoassay Systems, Weimar, Germany) at 70 °C to immobilize the MNP. Further details on the preparation method are found within this special issue in reference [36].

3.3 Simulation input

All simulation input parameters were chosen to match the experimental input parameters for magnetite MNP, as listed in Table 2.

Table 2. Simulation input parameters applied in the micromagnetic simulation model.

Effective anisotropy constant[a]	Saturation magnetization M_s	Mass density of Magnetite	Static field H_0	Excitation frequencies f_1 and f_2	Excitation amplitudes H_1 and H_2	Viscosity of surrounding (water)	Temperature
11 kJ/m³	476 kA/m	5.2 g/cm³	$(0, \ldots, 24)$ mT/μ_0; step size 1 mT/μ_0	136 Hz 40 545 Hz	14.55 mT/μ_0 1.25 mT/μ_0	$8.9 \cdot 10^{-4}$ Pa·s	310 K

[a] The literature value for bulk magnetite from [37] was used. Please find a short discussion explaining why we chose this value as the last paragraph in the discussion (section 5).

The damping parameter α was set to unity [38]. Simulations were carried out with Brownian rotation enabled and disabled (modelling freely suspended and immobilized MNP, respectively). Using a very narrow size distribution of $\sigma = 0.05$ and mean core sizes of $d_0 = (10,15,20,25,30)$ nm as input for the relaxation dynamics simulations, we are able to generate the FMMD-signal isolatedly for a specific size-fraction of MNP. The narrow size distribution is chosen according to approximate the most monodisperse (narrow) MNP size distributions synthesizable at present [28,39].

4 Results

4.1 Experimental results from FMMD measurements

Figure 1 shows the first four demodulations for $f_1 + nf_2$; $n = \{1,2,3,4\}$ for both Perimag and Nanomag MNP suspended in water (Brownian & Néel relaxation allowed) and immobilized on filter columns (only Néel relaxation allowed). The data is normalized to the single highest intensity, occurring at an offset field $H_0 = 13$ mT/μ0 in the first demodulation $f_1 + f_2$ for MNP in suspension in both samples.

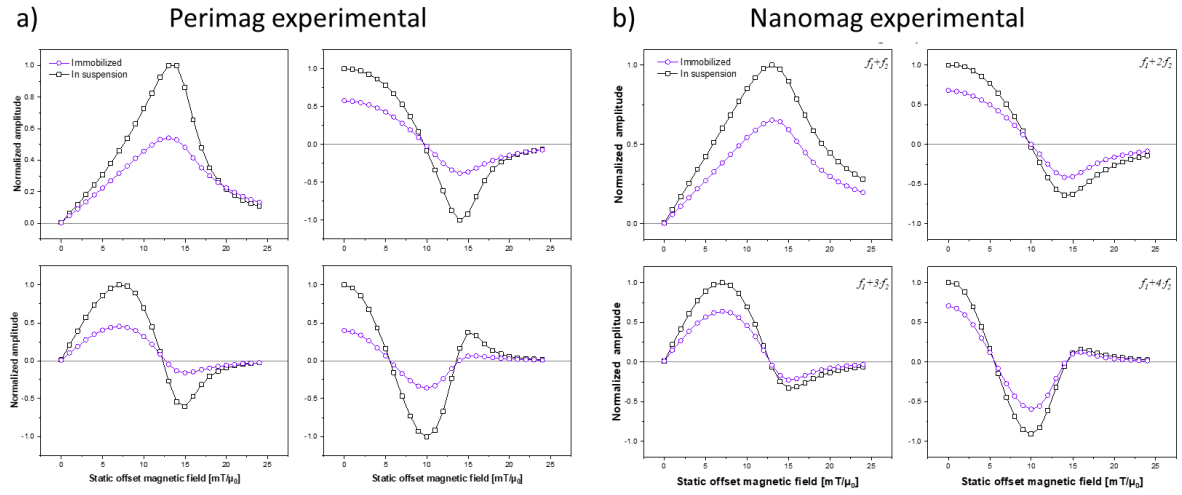

Figure 1: Experimental non-linear magnetic moment for (a) Perimag and (b) Nanomag MNP detected after dual frequency excitation at mixing frequencies $f_1 + n \cdot f_2$ with $n = 1,2,3,4$ for immobilized and freely suspended (water) samples. Lines are meant to guide the eye.

As can be easily seen from Figure 1, the FMMD signal is substantially diminished for immobilized MNP, which amounts to a decrease in the maximum of the first demodulation $f_1 + f_2$ on approx. 45% for Perimag and approx. 30% for Nanomag. From a direct comparison between the two samples, one observes furthermore that Perimag MNP show generally sharper and more pronounced peaks in all four demodulations.

4.2 Predicted results from relaxation dynamics simulations

The relaxation dynamics simulated results predicting the FMMD signal for specific core size fractions are shown exemplarily for Perimag MNP in suspension (Figure 2a) and immobilized (Figure 2b). The data is normalized to the single highest intensity, occurring at an offset field $H_0 = 13$ mT/μ0 for $d_0 = 30$ nm in the first demodulation $f_1 + f_2$ for MNP in suspension. Simulation data on Nanomag MNP can be found in Appendix A, Figure A1, which does show the exact same trends as seen for Perimag MNP, to be discussed later in section 5.

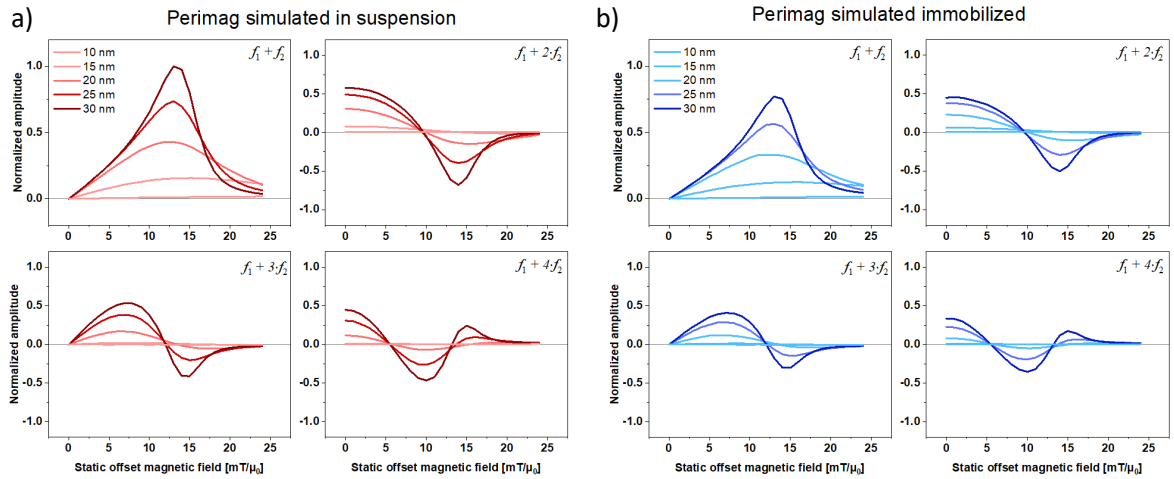

Figure 2: Simulated non-linear magnetic moment for Perimag MNP (a) in suspension and (b) immobilized for dual frequency excitation at mixing frequencies $f_1 + n \cdot f_2$ with $n = 1,2,3,4$ with specific core size fractions of mean core sizes $d_0 = \{10, \dots, 30\}$ nm. Normalized to the highest total intensity.

Figure 2 allows the following observations from comparison:

- Larger mean core size distributions generally generate stronger FMMD signals.
- 10 nm mean core size distributions do not contribute to the signal at all.
- The decrease in signal intensity for smaller mean core size distributions is more prominent for MNP in liquid suspension compared to immobilized MNP (cf. e.g. $d_0 = 20$ nm; $f_1 + f_2$ and $f_1 + 2f_2$).
- For identical field and MNP properties, MNP in suspension generate a stronger signal than immobilized MNP; e.g. specifically for $f_1 + f_2$ and $d_0 = 30$ nm (where the effect is strongest) the decrease for immobilized MNP compared to freely suspended MNP is 25%.

4.3 Consolidating experimental and simulated results

In order to decide which specific size-fraction is actually applicable to either of the experimental MNP samples (Perimag and Nanomag), we calculated the respective size distributions according to the log-normal size distribution with a probability density function (PDF) given by [40]:

$$\mathrm{PDF}(d_c, d_0, \sigma) = \frac{1}{\sqrt{2\pi} \cdot d_c \cdot \sigma} \cdot \exp\left(-\frac{\ln^2(d_c/d_0)}{2\sigma^2}\right), \tag{5}$$

using $d_0 = 19$ nm for Perimag [41] and $d_0 = 9$ nm for Nanomag [42,43], both with a distribution width of $\sigma = 0.3$ in accordance with literature [17,42,44] and manufacturer data (Table 1). Figure 3 shows a comparison of these PDF for the experimentally used MNP to those distributions with input parameters used for simulations as described above. The PDFs are weighted to the number of particles.

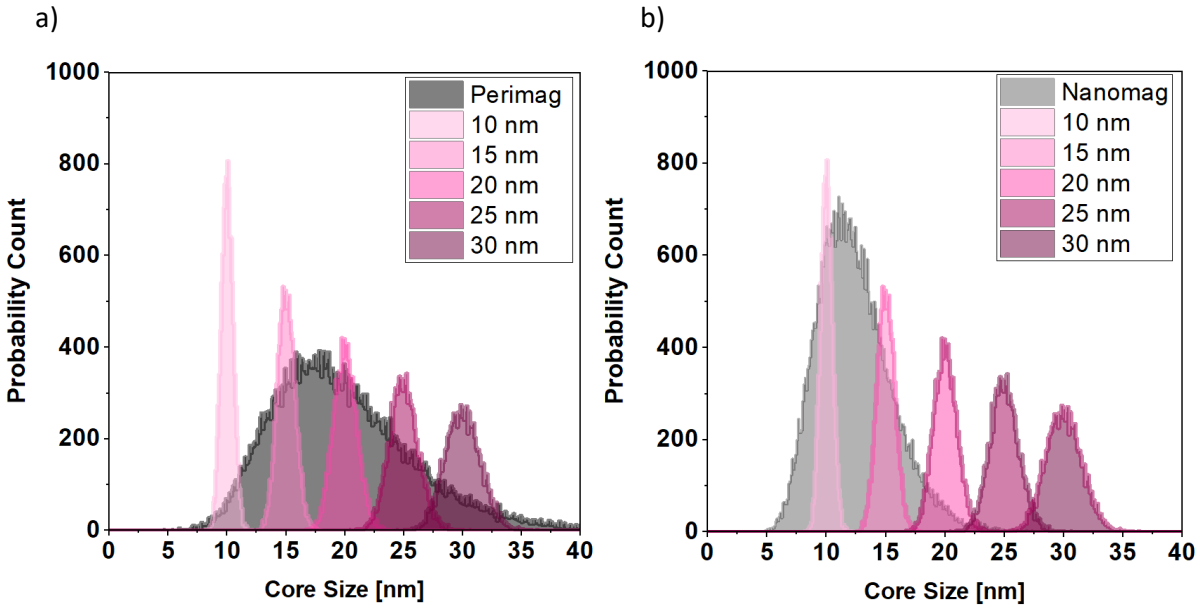

Figure 3: Number-weighted probability density for (a) Perimag MNP ($d_0 = 19$ nm; $\sigma = 0.3$) and (b) Nanomag MNP ($d_0 = 9$ nm; $\sigma = 0.3$) compared to five different mean core sizes fractions (given in legend) of narrow distribution width ($\sigma = 0.05$). Perimag and Nanomag are calculated for 50,000 particles; simulated size-fractions for 10,000 particles each (i.e. total areas under the curve are equal for experimental vs. simulated distributions).

Figure 3 clearly indicates that Perimag MNP comprise a broad distribution of core sizes up to well above $d_C = 35$ nm, with the most particles ranging in sizes of $d_C \approx (15 - 20)$ nm. Contrastingly, Nanomag MNP display a narrower size distribution peaking at sizes $d_C \approx (10 - 12)$ nm with the largest particles measuring $d_C \approx 25$ nm.

From comparison to the overlaying distributions of the simulated size fractions, one sees directly that the contributions of $d_0 = 30$ nm shall be discarded for Nanomag, as there is no overlap. Furthermore, taking into account that simulation showed no contribution to signal generation for $d_0 = 10$ nm in both Perimag and Nanomag (s. section 4.2; Figure 2), we henceforth use simulations with $d_0 = \{15,20,25,30\}$ nm and $d_0 = \{15,20,25\}$ nm to describe Perimag and Nanomag MNP, respectively.

For qualitative comparison of measured and predicted FMMD signal generation, Figure 4a exemplarily shows the experimentally measured data for immobilized Perimag MNP together with the simulated data for size fractions with $d_0 = \{15,20,25,30\}$ nm. All data lines are normalized to their individual highest value, therefore only allowing qualitative comparison of trends. Comparing simulated size fractions to experimental data, one sees that $d_0 = 15$ nm does neither resemble the shape nor contribute substantially to the experimental signal. For the other size fractions, one observes that $d_0 = 25$ nm qualitatively resembles the experimental data best across all four demodulations, while $d_0 = \{20,30\}$ nm frames the experimental data generally well.

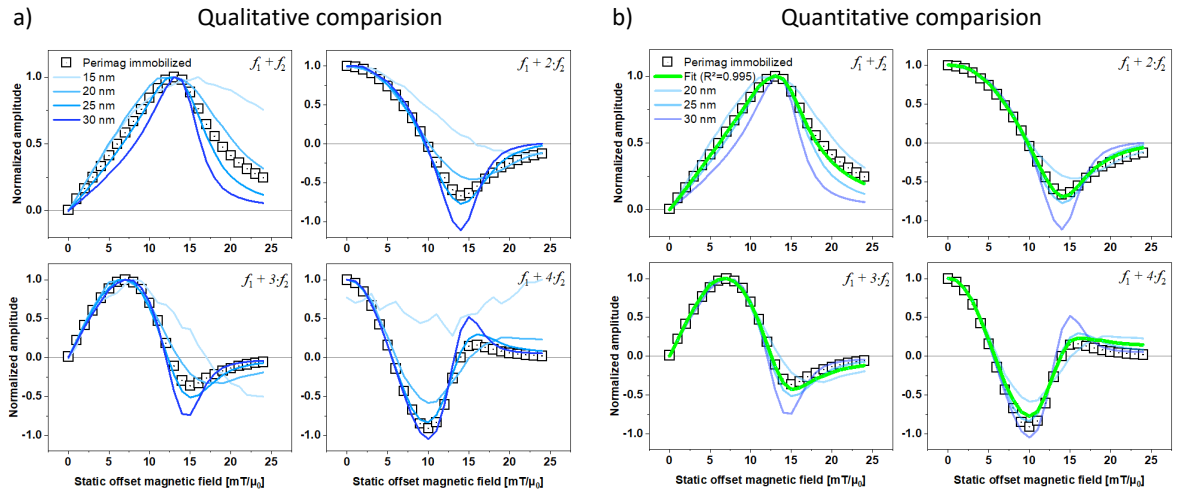

Figure 4: Non-linear magnetic moment for dual frequency excitation at mixing frequencies $f_1 + n \cdot f_2$ with $n = 1,2,3,4$ for immobilized perimag MNP for (a) qualitative comparison of experimental (open squares) and simulated data (solid lines) and (b) quantitative comparison showing the best fitting linear combination of simulated (transparent lines) to experimental data. Contributions for $d_0 = 15$ nm is excluded from (b) as the linear contribution is negligible (s. Table 3). For comparison, all data-lines are individually normalized to itself.

In order to also allow quantitative comparison of simulations to measured data, we use least-square fitting to determine the most suitable linearly-weighted combination of the simulated size fraction signal, A_{sim,d_0} (section 4.2), to the experimental data, A_{ex} (section 4.1):

$$A_{\mathrm{ex}} = \sum_{d_0} a_{d_0} \cdot A_{\mathrm{sim},d_0}, \qquad (6)$$

with $d_0 = \{15,20,25,30\}$ nm for Perimag and $d_0 = \{15,20,25\}$ nm for Nanomag. Figure 4b shows the fitting exemplarily for immobilized Perimag MNP with very good agreement derived across all four first demodulations ($n = \{1,2,3,4\}$) of $R^2 = 0.995$. The contributions of each simulated size fraction to the experimentally measured FMMD signal from fitting, a_{d_0}, for Perimag and Nanomag-D, in liquid suspension and immobilized, are listed in Table 3.

Table 3. Fitting parameters from least-square fitting size-fraction contributions from simulation to experimentally measured FMMD signal for $d_0 = \{15,20,25,30\}$ nm (Perimag) and $d_0 = \{15,20,25\}$ nm (Nanomag) for all samples.

Sample:	$a_{15\mathrm{nm}}$ [%]	$a_{20\mathrm{nm}}$ [%]	$a_{25\mathrm{nm}}$ [%]	$a_{30\mathrm{nm}}$ [%]	R^2
Perimag in suspension	<0.1	38.2	14.5	47.3	0.9921
Perimag immobilized	<0.1	46.0	27.7	24.3	0.9953
Nanomag in suspension	41.1	34.4	24.5	N/A	0.9957
Nanomag immobilized	36.6	33.6	29.8	N/A	0.9950

With $a_{15\mathrm{nm}} < 0.1$ for Perimag, the fitting corroborates the qualitative observation made from Figure 4a that contributions from size fractions with $d_0 = 15$ nm are not contributing to the measured FMMD signal. Furthermore, fitting suggests for suspended Perimag MNP that the

largest contribution to the measured FMMD signal stems from the size fraction of large particles with $d_0 = 30$ nm (47.3%), followed by mid-size particles with $d_0 = 20$ nm (38.2%), with $d_0 = 25$ nm showing only minor contributions (14.5%). Contrastingly, for immobilized Perimag MNP, the order is reversed: the largest contribution stems from the mid-size particles with $d_0 = 20$ nm (46.0%), followed almost evenly by $d_0 = 25$ nm (27.7%) and $d_0 = 30$ nm (24.3%).

For Nanomag MNP we observe identical trends for suspended and immobilized samples in the fitted size-dependent contribution to FMMD signal generation with $a_{20\mathrm{nm}}(\approx (36-41)\%) > a_{25\mathrm{nm}}(\approx 34\%) > a_{30\mathrm{nm}}(\approx (25-30)\%)$. As will be discussed in section 5, we attribute relative independence on the binding state to the intrinsic microstructure of individual Nanomag MNP.

5 Discussion

Our results confirm that larger particles dominantly contribute to the FMMD signal generation as previous research literature suggests [33,45]. This assumption is confirmed by extensively investigated results for other prominent biomedical applications of MNP, rating $d_0 \sim 25$ nm favorable for MPI signal generation [18,46] as well as heat generation for therapeutic MFH application [27,47]. Both theory and experiment predict the best results for close-to-superparamagnetic-limit sized magnetite particles ($d_0 \sim 25$ nm). Such monodisperse particles remain a general challenge in particle synthesis for many labs and for commercially available MNP formulations [43]: Especially for co-precipitation synthesis, broad size distributions spanning a range of up to 20 nm are still commonly found [17]. To improve FMMD applicability and sensitivity as a competitive biosensing procedure, it is therefore critical to quantify the exact contribution of each individual MNP systems size distribution to the overall FMMD signal generation. This quantification could then guide towards the most suitable MNP systems depending on the specific application.

The presented method of using advanced magnetic relaxation simulations to predict the FMMD signal of size-fractions of MNP and fitting these to experimental data allows to directly quantify the specific size-dependent contributions to the overall signal, as summarized in Table 3. At first sight, our study corroborates generally that larger MNP with core sizes $d_C \geq 15$ nm generate the FMMD signal, as shown previously [33]. At a closer look of the analyzed MNP systems, however, there is more insight to be gained: The contribution of $d_0 = 15$ nm size fraction is dominant in Nanomag MNP ($(36-41)\%$) while it is negligible in Perimag MNP. Furthermore, Perimag MNP shows the strongest contribution to the signal for the largest size fraction with $d_0 = 30$ nm (47.3%) when freely suspended but recedes to dominant contribution for $d_0 = 20$ nm (46.0%) when immobilized. The former observation can be explained by the size distribution of the MNP samples, while the latter is addressed in terms of the availability of Brownian relaxation in the samples. Additionally, both phenomena can be linked to the specific microstructural arrangements of the MNP, as will be outlined in the following.

As Figure 3 depicts, Nanomag MNP are more narrowly distributed, dropping to insignificant amounts of MNP with $d_C > 25$ nm, while for Perimag, a substantial fraction of MNP with sizes $d_C > 30$ nm are expected. As the fitting process (section 4.3) also takes the quantitative availability of MNP per sample into account, the fitting results (Table 3) confirm the natural assumption that for each MNP sample, the best combination of availability and core size is chosen. Therefore, knowledge of the MNP size distribution is indispensably important for the future design of ideal MNP-markers in FMMD-based immunoassays [35,48,49]. However, if

such knowledge is inaccessible for any reason, the method presented in this work allows for a quantitative analysis.

It is noteworthy that Nanomag MNP do not show a remarkable change in size fraction contributions for freely suspended versus immobilized particles, while Perimag does (i.e. shifting from dominant contribution for the largest fraction $d_0 = 30$ nm for freely suspended towards a mid-size fraction $d_0 = 20$ nm for immobilized (cf. Table 3). This observation can be explained in terms of the different microstructure of the samples: From XRD and SANS analysis, Nanomag MNP are confirmed to have its particles cores individually bound inside the dextran matrix [42]. With knowing the mean core size $d_0 = 9$ nm, which is generally expected to relax Néel-dominated [50], an immobilization-independent trend in size-fraction contributions seems reasonable for Nanomag. Contrastingly, Perimag MNP have generally larger cores ($d_0 = 19$ nm) and are furthermore prone to clustering (see manufacturer's data sheet and [51]), we expect a generally Brownian-dominated relaxation mechanism, especially since clustering is known to potentially increase the effective magnetic anisotropy constant and thereby further favoring Brownian relaxation contributions [52,53]. Therefore, it seems again reasonable that Perimag in suspension is predicted dominant contributions for large size-fractions with $d_0 = 30$ nm, which also enables clusters to generate the signal. For immobilized MNP on the contrary, Brownian contributions of large single particles and especially clusters are cut back and the dominant contribution derived from fitting stems from the size-fraction $d_0 = 20$ nm.

The drop in FMMD signal for immobilized MNP compared to freely suspended MNP is experimentally found to be $\approx (30 - 45)\%$ (Figure 1) and $\approx 25\%$ in simulation (Figures 2 and 1A) in both particle systems. This can be explained by the blocking of the Brownian relaxation mechanism, as both samples are expected to show significant Brownian contributions due to their significant content of large-core particles with $d_c \geq 15$ nm and their large hydrodynamic sizes of $d_H \geq 100$ nm (Table 1) [1,16]. A comparable effect has been reported experimentally for MFH applications, where MNP heating ability was demonstrated to drop by $\sim$35% for MNP with $d_0 = 9$ nm [54] and by $\sim$50% for MNP with $d_0 = (12 - 15)$ nm [55] upon particle immobilization, both attributed to a total blockade of Brownian rotation. The discrepancy in experimentally and simulated decrease in our comparison might arise from excluding particle-particle interactions in simulations, which, however, are suggested to dominate in dried samples as our immobilized MNP and could further increase the effective anisotropy constant, as outlined in the former paragraph. Potentially, it would therefore be of interest to integrate clustering effects in future simulations [56] to further investigate this hypothesis.

Lastly, the effective magnetic anisotropy constant, K_{eff}, is generally dependent on the MNP core size, as for such a high surface-to-volume ratio, the crystal symmetry at the surface is broken by structural defects and broken exchange bonds [57]. The exact impact of core size on anisotropy, however, is still under discussion, with evidence for either an increase (e.g. [58]) or decrease (e.g. [59]) in K_{eff} with increasing core size [60]. To deliberately excluded this discussion from the present study, we have therefore fixed the value of effective magnetic anisotropy to $K = K_{\mathrm{eff}} = 11$ kJ/m³ in our current simulations (s. Table 2). This value represents magnetite bulk value and is commonly accepted as a valid (starting) assumption to model K_{eff} [16]. However, we plan to see beyond this current limitation in our study design by varying K values and probing its impact on FMMD signal generation in future simulation-based studies.

6 Conclusions

We report on correlating experimental FMMD measurements on Perimag ($d_0 = 19$ nm) and Nanomag ($d_0 = 9$ nm) MNP systems with non-linear Néel-Brown magnetic relaxation dynamics simulations of different narrow size-fractions with $d_0 = \{10,15,20,25,30\}$ nm. In addition, MNP are prepared and simulated in suspension and immobilized. Experiment and simulation support the same conclusions, independently and for each of the MNP systems individually, as follows:

- First, that large particles ($d_0 = 30$ nm) contribute strongest to the FMMD signal generation.
- Second, that the underlying size distribution of the MNP must also be taken into account, regulating the quantitative contribution of each size-fraction.
- Third, that blocking Brownian contributions by particle immobilization causes a decrease in FMMD signal by approx. 25%.

By using weighted-fitting of results for simulated size-fraction to the measured FMMD signal, it is possible to quantify the size fraction that is majorly generating the FMMD signal under specific field and MNP conditions, which even allows to draw conclusions about the MNP microstructure and intraparticle arrangement (e.g. individually arranged MNP bound in matrix or potentially clustered cores). Such quantifications will allow to further fine-tune FMMD setup parameters (excitation amplitudes and frequencies) on the one hand, and specific MNP properties (mean core size, size distribution and other factors such as the magnetic anisotropy constant [16,61]) on the other hand, in order to advance FMMD utility in general and biosensing applicability in specific.

As outlined in section 5.1, the presented work also generally demonstrates the capability and versatility of using advanced magnetic relaxation simulations to predict the FMMD signal generation along the following effects:

- Reasonably predicting FMMD signal for two independent MNP systems; allowing assumptions about the underlying microstructure (individual MNP vs clusters)
- Reproducibly and comprehensively deriving size-fraction dependent contributions to the signal in accordance with experimental size distributions
- Resolving remarkable differences in the signal due to blocking of Brownian relaxation contributions for immobilized MNP in accordance with literature

We have presented a comprehensive prediction of FMMD signals using micromagnetic relaxation simulations. In comparison to previous comparative modelling of simulated vs experimental FMMD signals (cf. [33]), it seems majorly important to choose the exact experimental field parameters for simulation input to calculate correct results. We consider our current results as a cornerstone to design solely simulation-based field-and MNP-properties-dependent studies to further investigate and thereby reliably predict the ideal conditions for most sensitive FMMD biosensing application.

Appendix

Appendix A: Simulated prediction of FMMD signal for Nanomag MNP

Figure A1 shows simulated size-dependent FMMD signal intensity for Nanomag MNP (a) in suspension and (b) immobilized. The data is normalized to the single highest intensity,

occurring at an offset field $H_0 = 13$ mT/μ0 for $d_0 = 30$ nm in the first demodulation $f_1 + f_2$ for MNP in suspension. The decrease in FMMD signal between freely suspended and immobilized MNP amounts to 24,0% for $f_1 + f_2$ and $d_0 = 30$ nm.

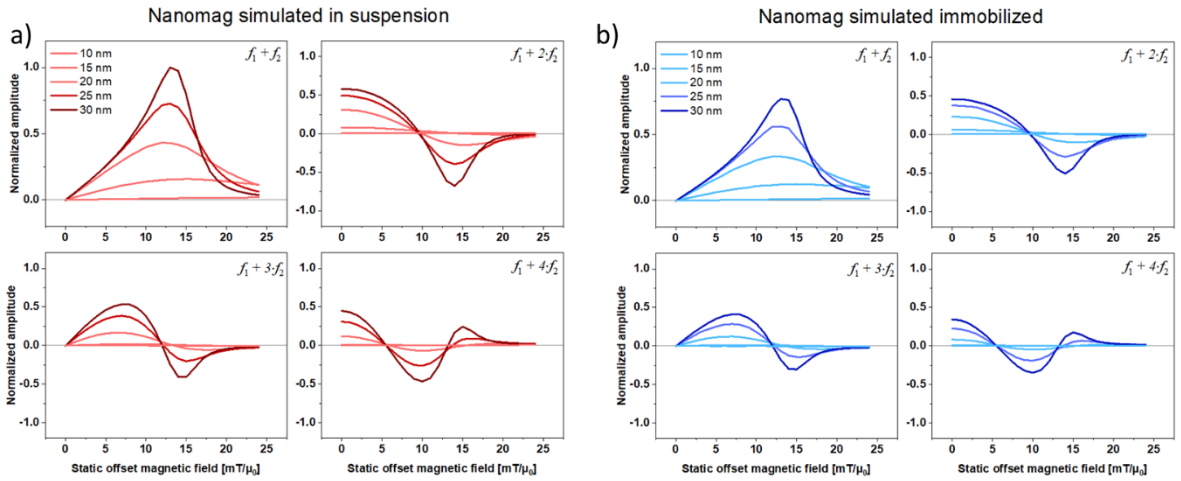

Figure A1: Simulated non-linear magnetic moment for Nanomag MNP (a) in suspension and (b) immobilized for dual frequency excitation at mixing frequencies $f_1 + n \cdot f_2$ with $n = 1,2,3,4$ with specific core size fractions of mean core sizes $d_0 = \{10, \ldots, 30\}$ nm. Normalized to the highest total intensity.

Acknowledgements

The authors deeply thank K.M. Krishnan and C. Shasha from University of Washington, Seattle, USA for collaboration on the original source code. Simulations were performed with computing resources provided by FH Aachen University of Applied Sciences, Dept. of Medical Engineering and Applied Mathematics, under guidance of Martin Reißel.

Funding

U.E. was funded by German Federal Ministry of Culture and Science of North Rhine-Westphalia, grant Karrierewege FH-Professur.

Conflicts of Interest

The authors declare no conflict of interest. The funders had no role in the design of the study; in the collection, analyses, or interpretation of data; in the writing of the manuscript, or in the decision to publish the results.

Data Availability Statement

The data presented in this study are available on request from the corresponding authors. Source code used for the nonlinear particle relaxation dynamics simulations can be accessed here https://github.com/cshasha/nano-simulate.

References

References

[1] K.M. Krishnan, Biomedical nanomagnetics: a spin through possibilities in imaging, diagnostics, and therapy, IEEE Trans. Magn. 46 (2010) 2523–2558.

[2] S.M. Dadfar, D. Camozzi, M. Darguzyte, K. Roemhild, P. Varvarà, J. Metselaar, S. Banala, M. Straub, N. Güvener, U. Engelmann, Size-isolation of superparamagnetic iron oxide nanoparticles improves MRI, MPI and hyperthermia performance, Journal of nanobiotechnology 18 (2020) 1–13.

[3] P.B. Kharat, S.B. Somvanshi, K.M. Jadhav, Multifunctional magnetic nano-platforms for advanced biomedical applications: a brief review, in: Journal of Physics: Conference Series, IOP Publishing, p. 12036.

[4] U.M. Engelmann, Assessing Magnetic Fluid Hyperthermia: Magnetic Relaxation Simulation, Modeling of Nanoparticle Uptake inside Pancreatic Tumor Cells and in vitro Efficacy, first ed., Infinite Science Publication, Lübeck, 2019.

[5] R. Chantrell, J. Popplewell, S. Charles, Measurements of particle size distribution parameters in ferrofluids, IEEE Trans. Magn. 14 (1978) 975–977.

[6] P. Chandrasekharan, Z.W. Tay, D. Hensley, X.Y. Zhou, B.K.L. Fung, C. Colson, Y. Lu, B.D. Fellows, Q. Huynh, C. Saayujya, Using magnetic particle imaging systems to localize and guide magnetic hyperthermia treatment: tracers, hardware, and future medical applications, Theranostics 10 (2020) 2965.

[7] Y. Lu, A. Rivera-Rodriguez, Z.W. Tay, D. Hensley, K.B. Fung, C. Colson, C. Saayujya, Q. Huynh, L. Kabuli, B. Fellows, Combining magnetic particle imaging and magnetic fluid hyperthermia for localized and image-guided treatment, International Journal of Hyperthermia 37 (2020) 141–154.

[8] Z.W. Tay, P. Chandrasekharan, A. Chiu-Lam, D.W. Hensley, R. Dhavalikar, X.Y. Zhou, E.Y. Yu, P.W. Goodwill, B. Zheng, C. Rinaldi, Magnetic particle imaging-guided heating in vivo using gradient fields for arbitrary localization of magnetic hyperthermia therapy, Acs Nano 12 (2018) 3699–3713.

[9] K. Kriz, J. Gehrke, D. Kriz, Advancements toward magneto immunoassays, Biosensors and Bioelectronics 13 (1998) 817–823.

[10] J. Lange, R. Kötitz, A. Haller, L. Trahms, W. Semmler, W. Weitschies, Magnetorelaxometry—A new binding specific detection method based on magnetic nanoparticles, Journal of Magnetism and Magnetic Materials 252 (2002) 381–383.

[11] H.-J. Krause, N. Wolters, Y. Zhang, A. Offenhäusser, P. Miethe, M.H.F. Meyer, M. Hartmann, M. Keusgen, Magnetic particle detection by frequency mixing for immunoassay applications, Journal of Magnetism and Magnetic Materials 311 (2007) 436–444.

[12] S. Achtsnicht, Multiplex magnetic detection of superparamagnetic beads for the identification of contaminations in drinking water, Dissertation, RWTH Aachen University, Aachen, 2020.

[13] K. Wu, R. Saha, D. Su, V.D. Krishna, J. Liu, M.C.-J. Cheeran, J.-P. Wang, Magnetic-nanosensor-based virus and pathogen detection strategies before and during covid-19, ACS Applied Nano Materials 3 (2020) 9560–9580.

[14] J. Pietschmann, D. Dittmann, H. Spiegel, H.-J. Krause, F. Schröper, A Novel Method for Antibiotic Detection in Milk Based on Competitive Magnetic Immunodetection, Foods 9 (2020) 1773.

[15] S. Achtsnicht, C. Neuendorf, T. Faßbender, G. Nölke, A. Offenhäusser, H.-J. Krause, F. Schröper, Sensitive and rapid detection of cholera toxin subunit B using magnetic frequency mixing detection, PloS one 14 (2019) e0219356.

[16] K.M. Krishnan, Fundamentals and applications of magnetic materials, Oxford University Press, 2016.

[17] N.T.K. Thanh, Magnetic nanoparticles: from fabrication to clinical applications, 14398693 (2012).

[18] C. Shasha, E. Teeman, K.M. Krishnan, Nanoparticle core size optimization for magnetic particle imaging, Biomedical physics & engineering express 5 (2019) 55010.

[19] E.Y. Yu, M. Bishop, B. Zheng, R.M. Ferguson, A.P. Khandhar, S.J. Kemp, K.M. Krishnan, P.W. Goodwill, S.M. Conolly, Magnetic particle imaging: a novel in vivo imaging platform for cancer detection, Nano letters 17 (2017) 1648–1654.

[20] C. Shasha, K.M. Krishnan, Nonequilibrium Dynamics of Magnetic Nanoparticles with Applications in Biomedicine, Adv. Mater. (2020) e1904131. https://doi.org/10.1002/adma.201904131.

[21] S. Ruta, R. Chantrell, O. Hovorka, Unified model of hyperthermia via hysteresis heating in systems of interacting magnetic nanoparticles, Sci. Rep. 5 (2015) 1–7.

[22] B. Mehdaoui, A. Meffre, J. Carrey, S. Lachaize, L.-M. Lacroix, M. Gougeon, B. Chaudret, M. Respaud, Optimal size of nanoparticles for magnetic hyperthermia: a combined theoretical and experimental study, Adv. Funct. Mater. 21 (2011) 4573–4581.

[23] E. Lima, E. de Biasi, M.V. Mansilla, M.E. Saleta, M. Granada, H.E. Troiani, F.B. Effenberger, L.M. Rossi, H.R. Rechenberg, R.D. Zysler, Heat generation in agglomerated ferrite nanoparticles in an alternating magnetic field, Journal of Physics D: Applied Physics 46 (2012) 45002.

[24] U.M. Engelmann, C. Shasha, I. Slabu, Magnetic nanoparticle relaxation in biomedical application: focus on simulating nanoparticle heating, Magnetic Nanoparticles in Human Health and Medicine: Current Medical Applications and Alternative Therapy of Cancer (2021) 327–354.

[25] C. Shasha, Nonequilibrium nanoparticle dynamics for the development of Magnetic Particle Imaging: PhD Thesis, 2019.

[26] P. Ilg, M. Kröger, Dynamics of interacting magnetic nanoparticles: effective behavior from competition between Brownian and Néel relaxation, Phys. Chem. Chem. Phys. 22 (2020) 22244–22259. https://doi.org/10.1039/d0cp04377j.

[27] U.M. Engelmann, C. Shasha, E. Teeman, I. Slabu, K.M. Krishnan, Predicting size-dependent heating efficiency of magnetic nanoparticles from experiment and stochastic

Néel-Brown Langevin simulation, Journal of Magnetism and Magnetic Materials 471 (2019) 450–456. https://doi.org/10.1016/j.jmmm.2018.09.041.

[28] E. Teeman, C. Shasha, J.E. Evans, K.M. Krishnan, Intracellular dynamics of superparamagnetic iron oxide nanoparticles for magnetic particle imaging, Nanoscale 11 (2019) 7771–7780. https://doi.org/10.1039/c9nr01395d.

[29] D. Cabrera, A. Coene, J. Leliaert, E.J. Artés-Ibáñez, L. Dupré, N.D. Telling, F.J. Teran, Dynamical Magnetic Response of Iron Oxide Nanoparticles Inside Live Cells, Acs Nano 12 (2018) 2741–2752. https://doi.org/10.1021/acsnano.7b08995.

[30] I. Rubia-Rodríguez, A. Santana-Otero, S. Spassov, E. Tombácz, C. Johansson, P. de La Presa, F.J. Teran, M.P. Del Morales, S. Veintemillas-Verdaguer, N.T.K. Thanh, Whither magnetic hyperthermia? A tentative roadmap, Materials 14 (2021) 706.

[31] T.L. Gilbert, Classics in Magnetics A Phenomenological Theory of Damping in Ferromagnetic Materials, IEEE Trans. Magn. 40 (2004) 3443–3449. https://doi.org/10.1109/TMAG.2004.836740.

[32] N.A. Usov, B.Y. Liubimov, Dynamics of magnetic nanoparticle in a viscous liquid: Application to magnetic nanoparticle hyperthermia, Journal of Applied Physics 112 (2012) 23901. https://doi.org/10.1063/1.4737126.

[33] U.M. Engelmann, A. Shalaby, C. Shasha, K.M. Krishnan, H.-J. Krause, Comparative Modeling of Frequency Mixing Measurements of Magnetic Nanoparticles Using Micromagnetic Simulations and Langevin Theory, Nanomaterials (Basel) 11 (2021). https://doi.org/10.3390/nano11051257.

[34] H. Hong, E.-G. Lim, J.-C. Jeong, J. Chang, S.-W. Shin, H.-J. Krause, Frequency Mixing Magnetic Detection Scanner for Imaging Magnetic Particles in Planar Samples, J. Vis. Exp. (2016). https://doi.org/10.3791/53869.

[35] A.M. Pourshahidi, S. Achtsnicht, M.M. Nambipareechee, A. Offenhäusser, H.-J. Krause, Multiplex Detection of Magnetic Beads Using Offset Field Dependent Frequency Mixing Magnetic Detection, Sensors 21 (2021) 5859.

[36] A.M. Pourshahidi, U.M. Engelmann, A. Offenhäusser, H.-J. Krause, Resolving ambiguities in core size determination of magnetic nanoparticles from magnetic frequency mixing data, Journal of Magnetism and Magnetic Materials (2022).

[37] H. Aali, S. Mollazadeh, J.V. Khaki, Single-phase magnetite with high saturation magnetization synthesized via modified solution combustion synthesis procedure, Ceramics International 44 (2018) 20267–20274.

[38] S.A. Shah, D.B. Reeves, R.M. Ferguson, J.B. Weaver, K.M. Krishnan, Mixed Brownian alignment and Néel rotations in superparamagnetic iron oxide nanoparticle suspensions driven by an ac field, Phys. Rev. B 92 (2015) 94438.

[39] S.J. Kemp, R.M. Ferguson, A.P. Khandhar, K.M. Krishnan, Monodisperse magnetite nanoparticles with nearly ideal saturation magnetization, RSC Adv. 6 (2016) 77452–77464. https://doi.org/10.1039/C6RA12072E.

[40] S.P. Gubin, Magnetic Nanoparticles, WILEY-VCH Verlag GmbH & Co, Weinheim, 2009.

[41] M. Irfan, N. Dogan, T. Sapmaz, A. Bingolbali, Development of MPI relaxometer for characterization of superparamagnetic nanoparticles, Journal of Magnetism and Magnetic Materials 536 (2021) 168082. https://doi.org/10.1016/j.jmmm.2021.168082.

[42] C.L. Dennis, K.L. Krycka, J.A. Borchers, R.D. Desautels, J. van Lierop, N.F. Huls, A.J. Jackson, C. Gruettner, R. Ivkov, Internal Magnetic Structure of Nanoparticles Dominates Time-Dependent Relaxation Processes in a Magnetic Field, Adv. Funct. Mater. 25 (2015) 4300–4311. https://doi.org/10.1002/adfm.201500405.

[43] M. Kallumadil, M. Tada, T. Nakagawa, M. Abe, P. Southern, Q.A. Pankhurst, Suitability of commercial colloids for magnetic hyperthermia, Journal of Magnetism and Magnetic Materials 321 (2009) 1509–1513. https://doi.org/10.1016/j.jmmm.2009.02.075.

[44] Grüttner C., Teller J., Schütt W., Westphal F., Schümichen C., Paulke BR., Preparation and Characterization of Magnetic Nanospheres for in Vivo Application, in: U. Häfeli, W. Schütt, J. Teller, M. Zborowski (Eds.), Scientific and Clinical Applications of Magnetic Carriers, Springer, Boston, 1997.

[45] S. Achtsnicht, A.M. Pourshahidi, A. Offenhäusser, H.-J. Krause, Multiplex Detection of Different Magnetic Beads Using Frequency Scanning in Magnetic Frequency Mixing Technique, Sensors 19 (2019) 2599.

[46] Z.W. Tay, D.W. Hensley, E.C. Vreeland, B. Zheng, S.M. Conolly, The relaxation wall: experimental limits to improving MPI spatial resolution by increasing nanoparticle core size, Biomedical physics & engineering express 3 (2017) 35003.

[47] S. Tong, C.A. Quinto, L. Zhang, P. Mohindra, G. Bao, Size-dependent heating of magnetic iron oxide nanoparticles, Acs Nano 11 (2017) 6808–6816.

[48] H.B. Hong, H.-J. Krause, I.H. Nam, C.J. Choi, S.W. Shin, Magnetic immunoassay based on frequency mixing magnetic detection and magnetic particles of different magnetic properties, Analytical methods 6 (2014) 8055–8058.

[49] K. Wu, J. Liu, V.K. Chugh, S. Liang, R. Saha, V.D. Krishna, M.C.J. Cheeran, J.-P. Wang, Magnetic Nanoparticles and Magnetic Particle Spectroscopy-based Bioassays: A 15-year Recap, Nano Futures (2022).

[50] J. Dieckhoff, D. Eberbeck, M. Schilling, F. Ludwig, Magnetic-field dependence of Brownian and Néel relaxation times, Journal of Applied Physics 119 (2016) 43903. https://doi.org/10.1063/1.4940724.

[51] K.H. Yeo, I. Rodrigo, R. Kuo, P. Chandrasekharan, B. Fellows, S. Conolly, Characterizing the performance of commercial magnetic particles for magnetic particle imaging. International Journal on Magnetic Particle Imaging, Vol 8 No 1 Suppl 1 (2022) (2022). https://doi.org/10.18416/IJMPI.2022.2203080.

[52] U.M. Engelmann, E.M. Buhl, S. Draack, T. Viereck, F. Ludwig, T. Schmitz-Rode, I. Slabu, Magnetic relaxation of agglomerated and immobilized iron oxide nanoparticles for hyperthermia and imaging applications, IEEE Magnetics Letters 9 (2018) 1–5.

[53] C.L. Dennis, R. Ivkov, Physics of heat generation using magnetic nanoparticles for hyperthermia, International Journal of Hyperthermia 29 (2013) 715–729.

[54] U.M. Engelmann, J. Seifert, B. Mues, S. Roitsch, C. Ménager, A.M. Schmidt, I. Slabu, Heating efficiency of magnetic nanoparticles decreases with gradual immobilization in hydrogels, Journal of Magnetism and Magnetic Materials 471 (2019) 486–494. https://doi.org/10.1016/j.jmmm.2018.09.113.

[55] R. Ludwig, M. Stapf, S. Dutz, R. Müller, U. Teichgräber, I. Hilger, Structural properties of magnetic nanoparticles determine their heating behavior-an estimation of the in vivo heating potential, Nanoscale research letters 9 (2014) 1–10.

[56] F.L. Durhuus, L.H. Wandall, M.H. Boisen, M. Kure, M. Beleggia, C. Frandsen, Simulated clustering dynamics of colloidal magnetic nanoparticles, Nanoscale 13 (2021) 1970–1981.

[57] G. Salazar-Alvarez, J. Qin, V. Sepelak, I. Bergmann, M. Vasilakaki, K.N. Trohidou, J.D. Ardisson, W.A. Macedo, M. Mikhaylova, M. Muhammed, Cubic versus spherical magnetic nanoparticles: the role of surface anisotropy, Journal of the American Chemical Society 130 (2008) 13234–13239.

[58] L.C. Branquinho, M.S. Carrião, A.S. Costa, N. Zufelato, M.H. Sousa, R. Miotto, R. Ivkov, A.F. Bakuzis, Effect of magnetic dipolar interactions on nanoparticle heating efficiency: implications for cancer hyperthermia, Sci. Rep. 3 (2013) 2887. https://doi.org/10.1038/srep02887.

[59] F. Bødker, S. Mørup, S. Linderoth, Surface effects in metallic iron nanoparticles, Physical review letters 72 (1994) 282.

[60] S. Oyarzún, A. Tamion, F. Tournus, V. Dupuis, M. Hillenkamp, Size effects in the magnetic anisotropy of embedded cobalt nanoparticles: from shape to surface, Sci. Rep. 5 (2015) 1–8.

[61] F. Ludwig, H. Remmer, C. Kuhlmann, T. Wawrzik, H. Arami, R.M. Ferguson, K.M. Krishnan, Self-consistent magnetic properties of magnetite tracers optimized for magnetic particle imaging measured by ac susceptometry, magnetorelaxometry and magnetic particle spectroscopy, Journal of Magnetism and Magnetic Materials 360 (2014) 169–173. https://doi.org/10.1016/j.jmmm.2014.02.020.